ADVANCED FUNCTIONAL MATERIALS
www.afm-journal.de

Materials Views
www.MaterialsViews.com

Effect of Annealing Temperature on Film Morphology of Organic–Inorganic Hybrid Pervoskite Solid-State Solar Cells

Amalie Dualeh, Nicolas Tétreault, Thomas Moehl, Peng Gao, Mohammad Khaja Nazeeruddin, and Michael Grätzel**

Organic–inorganic hybrid perovskites have attracted attention as successful light harvesting materials for mesoscopic solid-state solar cells and led to record breaking efficiencies. The photovoltaic performance of these devices is greatly dependent on the film morphology, which in turn is dependent on the deposition techniques and subsequent treatments employed. In this work the perovskite film is deposited by spin-coating a precursor solution of $PbCl_2$ and CH_3NH_3I (1 to 3 molar ratio) in dimethylformamide. Here, the role of the temperature used in the annealing process required to convert the as deposited solution into the perovskite material is investigated. It is found that the conversion requires sufficiently high temperatures to ensure the vaporization of solvent and the crystallization of the perovskite material. However, increasing the annealing temperature too high leads to the additional formation of PbI_2, which is detrimental to the photovoltaic performance. Furthermore, the effect of the annealing temperature on the film formation, morphology, and composition is examined and correlated with the photovoltaic performance and device working mechanisms.

1. Introduction

In the field of solar energy conversion, thin film solar photovoltaics have been the focus of research and development as a promising more cost-effective alternative to their silicon counterpart. This area of research extends over a wide range of concepts, materials and device mechanisms to achieve efficient sunlight harvesting.

There has been a recent surge of progress in the field of thin film solar cells focusing on the integration of three-dimensional organic-inorganic hybrid perovskites in solar cell devices. The role of these types of material is reportedly complex; primarily as high extinction light absorbers,[1,2] with additional contributions as hole[3] and electron transport material.[4,5] A multitude of different deposition techniques and device architectures have been reported using this class of materials, but there exist basic similarities. Typically the perovskite material is deposited or formed on a type of mesoporous metal oxide scaffold, including nanoparticulate TiO_2,[6–8] Al_2O_3,[4,5] ZrO_2[9,10] on top of which a hole transport material (HTM) is deposited. The most common HTM is the amorphous organic semiconductor spiro-MeOTAD[2,4,5,9,11] but high efficiencies have also been achieved with polymer type HTMs.[12–14] Furthermore hole conductor free devices have been reported where the gold back contact is thermally evaporated directly on top of the perovskite-sensitized mesoporous TiO_2 film.[7]

Due to the recent increase in attention, the properties of the perovskite-based hybrid materials have been intensively investigated. The general formula of these perovskite materials is RNH_3MX_3, where RNH_3 ($R = C_nH_{2n+1}$) is the organic component and MX_3 (M = metal such as Pb or Sn, X = I, Br, or Cl) is the inorganic component.[15] Unlike other composite materials where inorganic and organic components are often either randomly arranged or have short-range order, the hybrid perovskite class of materials display long-range order in the crystal structure.[16,17] They have long been of interest due to their unique optical, electronic and magnetic properties which can be further tailored by manipulation of the individual organic and inorganic components.[18–20]

The solution processability of the organic-inorganic perovskite material is one of its major advantages, the simplest method of deposition requiring only a simple heating step to convert the deposited precursor solution (consisting of the organic and inorganic components) to the crystalline perovskite form. The morphology, stoichiometry and crystallinity of the material greatly influences the overall photovoltaic device performance. As such the deposition technique of the material is of crucial importance, as demonstrated by Burschka et al.[8] and Bi et al.,[9] which also includes all the treatments and conditions the material is exposed to as part of and/or following the conversion to the final perovskite form. The quality and nature of the perovskite layer formed is critical for high efficiency solar cells. Recent reports have demonstrated PCEs of over 15% from a planar heterojunction perovskite solar cell[21] which is attributed to the formation of extremely uniform flat films of the mixed halide perovskite $CH_3NH_3PbI_{3-x}Cl_x$ by vapor deposition. This indicates that the perovskite absorbers can result in high

A. Dualeh, Dr. N. Tétreault, Dr. T. Moehl, Dr. P. Gao, Dr. M. K. Nazeeruddin, Prof. M. Grätzel
Laboratory of Photonics and Interfaces
Institute of Chemical Sciences and Engineering
École Polytechnique Fédérale de Lausanne
Station 6, 1015 Lausanne, Switzerland
E-mail: mdkhaja.nazeeruddin@epfl.ch;
michael.graetzel@epfl.ch

DOI: 10.1002/adfm.201304022

Table 1. Conversion temperature and associated time taken.

Temperature [°C]	Time Taken [h]
ambient[a)]	20
60	20
80	3
100	0.75
120	0.25
150	0.25
175	0.17
200	0.17

[a)]Ambient temperature consisted of room temperature at approximately 20 °C.

PCEs in the simplest planar device configuration, but is heavily dependent on the nature of the perovskite film formed.

In this work the $CH_3NH_3PbI_3$ perovskite used as light absorber is deposited onto to the $mTiO_2$ by spin-coating from a 1:3 molar ratio solution of $PbCl_2$ and CH_3NH_3I in dimethylformamide (DMF) following the procedure reported by Lee et al.[4] In the standard case these films are subsequently annealed at 100 °C for 45 min leading to the formation of the lead-iodide based perovskite material. Here, we investigate the effect and importance of the annealing temperature during the final conversion step, relating it to the perovskite film morphology and its influence on the device working mechanisms. These perovskite films formed are analyzed using ultraviolet-visible absorption spectroscopy, scanning electron microscopy (SEM) and X-ray diffraction (XRD) measurements. This exposes the role of the annealing temperature of the perovskite on its film composition and morphology. The variation of the annealing temperature during the perovskite conversion step was correlated with the photovoltaic performance of solid-state solar cells using spiro-MeOTAD as HTM and further examined by impedance spectroscopy (IS) to gain better understanding of the internal electrical parameters under working conditions.

2. Results and Discussion

For most of the techniques where the perovskite material is deposited from solution, a subsequent heat treatment of the film is required. This has the dual purpose of removing any excess solvent remaining in the film as well as facilitating the formation of the perovskite crystal structure. Contrary to the case when PbI_2 is used as a precursor as reported by Kim et al.[2] which requires only 10 minutes of heating at 100 °C to complete the conversion to the final perovskite form, when $PbCl_2$ is used the conversion is complete only after annealing the material for 45 minutes like reported by Lee et al.[4] We investigated the effect of the variation of the annealing temperature of the perovskite films after deposition by spin-coating. The conversion to the final perovskite was regarded as complete once the film showed a stable absorption profile resulting in a uniform black color. For low temperatures this conversion took considerably longer, 3 h at 80 °C relative to 45 min at 100 °C. At 60 °C, even when left for more than 20 h the conversion was not complete as indicated by poorer film coloration. In the case of high annealing temperatures (>150 °C) the conversion was observed to occur almost instantaneously and in the case for temperatures above 200 °C to quickly convert to yellow. The exact amount of time used for the annealing of the perovskite films at different temperatures is presented in **Table 1**.

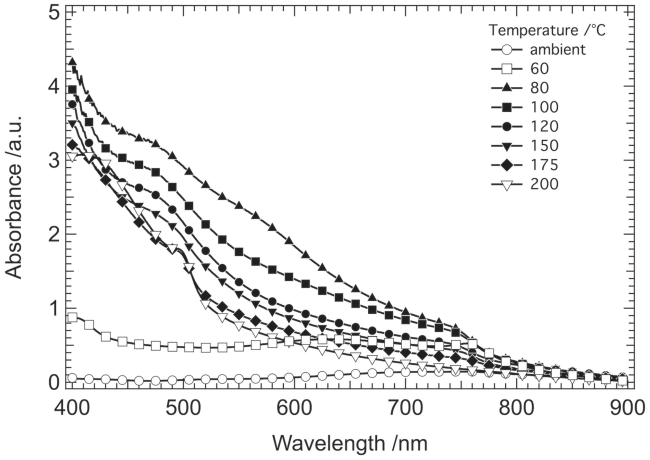

Figure 1. UV-vis absorption spectra for $mTiO_2$ films with perovskite annealed at different temperatures.

2.1. Ultraviolet-Visible Absorption

The ultraviolet-visible (UV-vis) absorption spectra of the perovskite material deposited on $mTiO_2$ and annealed at different temperatures are presented in **Figure 1**. The samples annealed at 80 to 150 °C show the typical absorption spectrum of the perovskite $CH_3NH_3PbI_3$ as reported.[1,4,7,11] Increasing the annealing temperature of the perovskite from 60 to 100 °C shows an increase in the absorbance across the entire spectral range, indicating that the extent of conversion is considerably lower at such low annealing temperatures. This is further highlighted by the extremely low absorbance of samples that were simply dried at ambient room temperatures without further heat-treatment. This latter case demonstrates that removal of the solvent from the film is insufficient to form the perovskite from these precursors and that energy is required to drive this conversion. This is confirmed by the lack of the features associated with the absorbance of PbI_2 corresponding to a peak at 500 nm or the perovskite absorption onset at 770 nm, which indicates that these dried precursor films contain only $PbCl_2$ and CH_3NH_3I.

The samples annealed at 80 °C show an additional absorption shoulder at 590 nm. The origin of this feature remains unclear. However it could be related to the broad absorption observed for the samples dried at 60 °C between 570 and 640 nm. Taking this exception into account the samples annealed at 100 °C showed the highest absorbance. Further increasing the annealing temperature leads not only to a decrease in absorbance but also the additional appearance of PbI_2 absorption feature at 500 nm (see Figure S1 Supporting Information for pure PbI_2 spectra). For samples heated at 200 °C the perovskite characteristics are almost no longer distinguishable and the spectra resembles that of pure PbI_2 with slightly higher

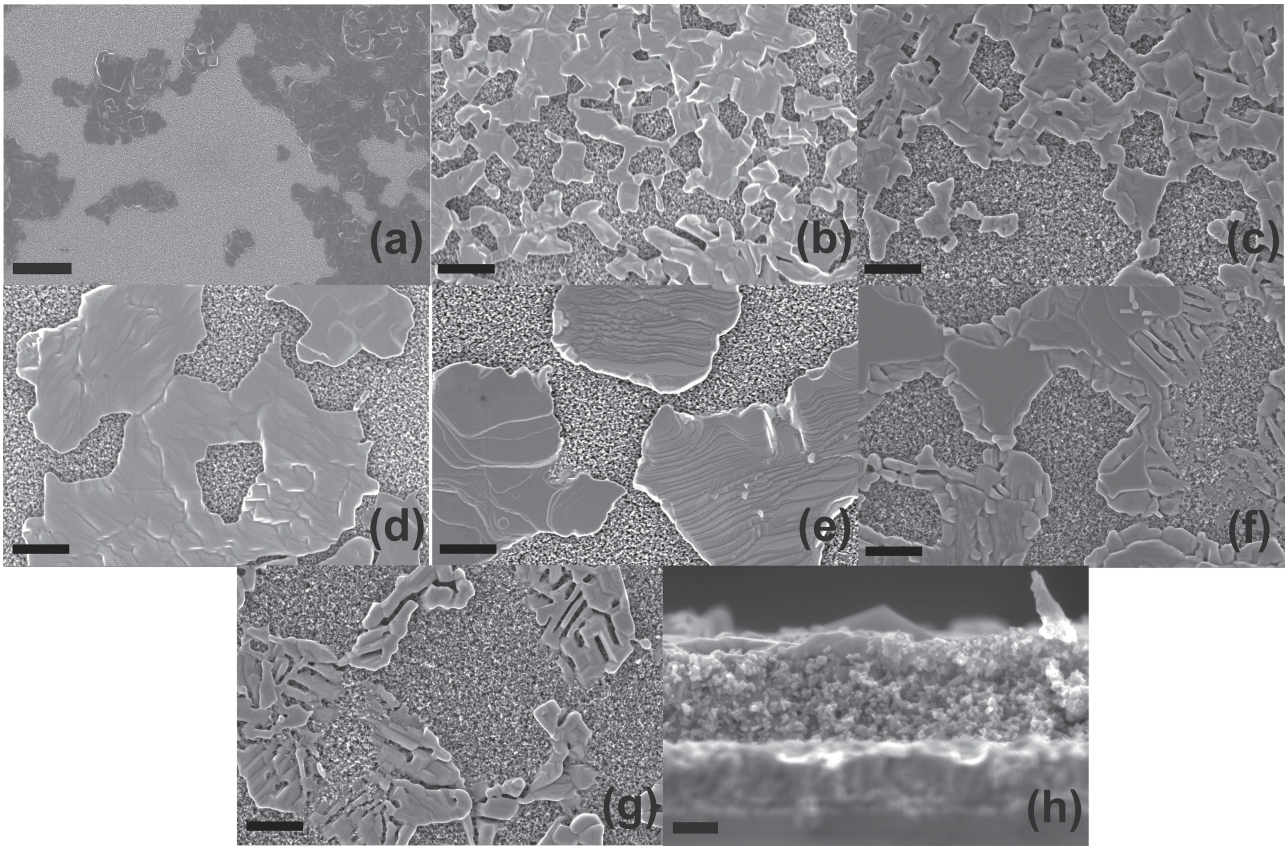

Figure 2. SEM images of $mTiO_2$ films with deposited perovskite solution heat treated at a) 60 °C, b) 80 °C, c) 100 °C, d) 120 °C, e) 150 °C, f) 175 °C, and g) 200 °C. h) Cross sectional image of sample annealed at 150 °C. Black scale bars correspond to a) 5 μm, b–g) 1 μm, and h) 200 nm.

light absorption between 600 and 800 nm. This confirms that the yellow colour of these films is due to the formation of PbI_2 at these high temperatures. This is in agreement with surface photovoltage spectroscopy measurements made by Supasai et al.[22] where the appearance of the PbI_2 bandgap after heating $CH_3NH_3PbI_3$ samples above 140 °C was observed. The absorption onset of the perovskite remains constant for samples annealed between 60 and 175 °C, indicating that the optical bandgap of the perovskite is unaffected by the annealing temperatures. This further confirms that the nature of the perovskite formed is unchanged by the annealing temperature and is found to be in good agreement with the $CH_3NH_3PbI_3$ perovskite. For the samples treated at ambient temperatures (where there is no formation of perovskite) or at very high temperatures (where the formation of PbI_2 is dominant), the perovskite bandgap absorption onset is not visible.

2.2. Scanning Electron Microscopy

The influence of the annealing temperature on the morphology and structure of the perovskite layer formed on the $mTiO_2$ were examined by scanning electron microscopy (SEM). For samples annealed at 60 °C no homogeneous film was formed, rather large islands of precursor material ($PbCl_2$ and CH_3NH_3I) are seen (**Figure 2**a). This is validated as the islands lack the clear crystalline structure typically observed for such perovskite materials. As the annealing temperature is increased to 80 °C there is a drastic change in the appearance of the film formed. The typical structure of the perovskite is visible. The coverage of the $mTiO_2$ is much higher and the shape of the individual crystallites is much better defined. The film formed upon annealing at 100 °C is relatively similar in appearance to that formed at 80 °C (Figure 2b,c) even though the time for the conversion process is longer at 80 °C. Furthermore, the gaps between the perovskite crystallites is slightly larger in the case of 100 °C. Increasing the annealing temperature to 120 °C the morphology of the perovskite adopts a larger individual size for the islands of material (Figure 2d). They no longer form a densely interconnected network, but rather larger islands with bigger gaps in between, resulting in seemingly larger uncovered $mTiO_2$ areas. Here is important to note that it is believed that these "exposed $mTiO_2$" areas are still covered by a thin layer of perovskite material, hence revealing the structure of the $mTiO_2$ underneath (see cross sectional image in Figure 2h).

As the annealing temperature is further increased, the size of perovskite islands becomes larger and furthermore internal structuring becomes discernable (Figure 2e–g). This is most extreme at the highest annealing temperature investigated (200 °C). Hence, Figure 2 clearly shows that the morphology of the perovskite film formed is significantly influenced by the annealing temperature.

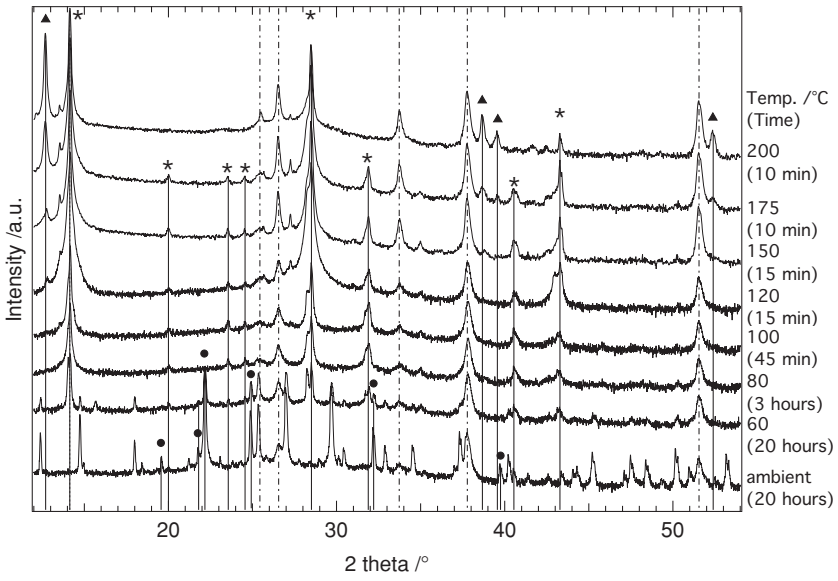

Figure 3. X-ray diffraction patterns of perovskite samples annealed at different temperatures. The perovskite was deposited on mesoporous TiO_2 coated onto FTO substrates. The vertical lines indicate the peaks associated with the perovskite material (stars), PbI_2 (triangles), $PbCl_2$ (circles), and the FTO/mTiO_2 substrate (dotted line). For clarity the same figure is presented in color in the Supporting Information, Figure S2.

As the annealing temperature is increased it can be assumed that the rate of perovskite crystallization is similarly increased. High temperatures resulted in the rapid growth from a few nucleation sites leading to the formation of large crystalline islands and the associated large gaps in between. Lower temperatures on the other hand allowed the formation and subsequent crystal growth from a large number of nucleation sites, leading to the formation of smaller islands.

2.3. X-Ray Diffraction

X-ray diffraction (XRD) measurements were conducted to investigate the nature of the material formed following the annealing process. As expected, low annealing temperatures result in the incomplete conversion to the perovskite (**Figure 3**). The XRD diffractograms for samples dried at ambient temperature for > 20 h exhibit a large number of peaks that are mainly attributed to the precursor materials. The presence of $PbCl_2$ peaks (indicated by circles in Figure 3 and in Figure S3 in Supporting Information) indicate that simply drying the films to remove the excess solvent is insufficient to convert the precursor solution to the desired perovskite material. In addition to the $PbCl_2$ peaks there are several peaks that remain unidentified. These could be attributed to the possible formation of products such as lead(II) oxychloride[23] arising due to the slow drying in the presence of water. Heating at 60 °C for > 20 h also still shows strong evidence of the presence of these precursor materials. However, in this case, a set of additional peaks appears (indicated by stars), matching those reported for the $CH_3NH_3PbI_3$ crystallized in the tetragonal perovskite structure.[7,24,25] The peaks at 14.17, 28.49, and 43.27° are respectively assigned to the (110), (220) and (330) planes. The presence of these peaks indicates that the conversion, while incomplete, does take place to a small extent at these low annealing temperatures.

If we recall the SEM image for the corresponding sample prepared at 60 °C, the islands of material observed can be confirmed to consist largely of dried precursors, with only a small proportion being converted to perovskite material. Once the annealing temperature is increased to 80 °C, the peaks for the precursors are no longer present and only the peaks for the perovskite material remain. As has been shown by Poglitsch et al.,[26] the $CH_3NH_3^+$ cation cannot be fixed in the crystal structure due to the disordered orientation and mobility of the cation in the crystal. As in the case of the SEM images, the XRD diffractograms for the sample annealed at 100 °C shows little difference to the 80 °C sample. As the annealing temperature is increased to 175 °C, the intensity of the perovskite (110), (220), and (330) peaks increases due to an increased conversion rate. From previous work it is known that this perovskite material shows a tendency for preferential orientation with the *a*-axis.[4,24,26,27] The increase in intensity of the reflections from the row of reciprocal lattice normal to the film plane suggests increased orientation of the perovskite crystalline domains with increases in annealing temperature. Similar observations were made for AlN films,[28] ZnO films prepared by sol-gel techniques and then exposed to different heat treatments[29] and FePt thin films with face-centered-tetragonal (001) texture.[30] Another origin of the observed increased intensity of the peak intensity may arise from the phenomenon of microabsorption, where larger crystallite phases preferentially interact with the diffracting beam, thus leading to a distortion of the diffraction intensities. For heat treatments at 200 °C the intensity of the perovskite is decreased and is explained by the decrease in material formed at these high temperatures.

In addition, for annealing temperatures above 120 °C a set of peaks that have been identified as belonging to PbI_2 appear.[8,31]

Hence, at lower temperatures, the conversion to the perovskite dominates following Reaction (), however at higher annealing temperatures, there is the additional formation of PbI_2 (Reaction 2).[22]

$$PbCl_2 + 3CH_3NH_3I \rightarrow CH_3NH_3PbI_3 + 2CH_3NH_3Cl \quad (1)$$

$$PbCl_2 + 3CH_3NH_3I \rightarrow PbI_2 + CH_3NH_3I + 2CH_3NH_3Cl \quad (2)$$

$$CH_3NH_3PbI_3 \rightarrow PbI_2 + CH_3NH_2 + HI \quad (3)$$

The perovskite crystal material has been reported to be stable up to 300 °C, at which point the organic component decomposes, leaving behind the inorganic PbI_2 following Reaction 3.[14,32] However recent studies[22] show that the $CH_3NH_3PbI_3$ perovskite begins to transform to PbI_2 at temperatures significantly below 300 °C (140 °C). In this study the perovskite is not yet

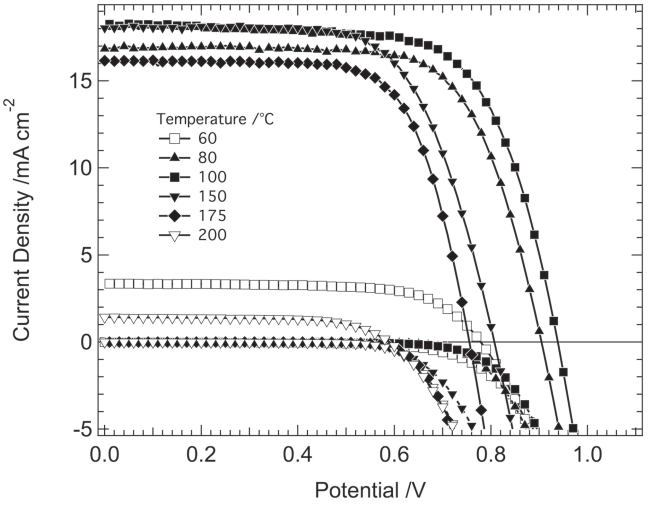

Figure 4. *J–V* characteristics taken under standard AM1.5G illumination (100 mW cm^{-2}) (solid) and in the dark (dashed) for devices made using different annealing temperatures for the perovskite.

formed prior to exposure to the annealing temperature and hence there are additional factors to consider. The excess organic CH_3NH_3Cl formed in this reaction is believed to sublime, thus leaving only the $CH_3NH_3PbI_3$ perovskite on the $mTiO_2$ film as observed in the XRD measurements. The rate of sublimation of the organic species CH_3NH_3Cl will increase with temperature, as will that of the precursor CH_3NH_3I, thus driving Reaction 2 in addition to Reaction 1. From these measurements it becomes evident that formation of the perovskite films is composed of multiple processes; solvent vaporization, perovskite crystallization and the sublimation of excess organic CH_3NH_3Cl need to take place. These processes occur simultaneously and their relative rates determine the composition of the final film and contribute to the different film morphologies observed in the SEM images above.

2.4. Photovoltaic Performance

Solid-state solar cells were fabricated using the perovskite as sensitizer and spiro-MeOTAD as hole-transport material. The perovskite material was deposited as described from solution containing a 1:3 molar ratio of $PbCl_2$ and CH_3NH_3I in DMF and annealed at different temperatures followed by the subsequent deposition of the hole-transport material (HTM) by spin-coating. The current-voltage (*J–V*) characteristics measured under standard AM1.5G illumination (100 mW cm^{-2}) of these devices are presented in **Figure 4**, the corresponding photovoltaic parameters of which are summarized in **Table 2**.

A clear correlation is observed between the annealing temperature of the perovskite and the photovoltaic performance of the devices. Samples that were annealed at 100 °C gave the highest power conversion efficiency (PCE), 11.66%, as a result of the highest open-circuit potential (V_{OC}) and short-current density (J_{SC}), 938 mV and 18.37 mA cm^{-2} respectively. At low annealing temperatures (60 °C) both of these parameters are decreased as a consequence of incomplete conversion to the perovskite material, leading to lower light harvesting as there is insufficient perovskite sensitizer present. The devices annealed at 80 °C displayed high PCE, and generally their parameters were only slightly lower than the maximum values observed at 100 °C. This is in agreement with the previous measurements that showed a large degree of similarity between samples prepared at 80 and 100 °C.

Table 2. Photovoltaic performance parameters extracted from *J–V* measurements under standard AM1.5G illumination (100 mW cm^{-2}) of devices using different annealing temperatures. All devices were masked to achieve an illuminated area of 0.285 cm^2.

Temperature [°C]	V_{OC} [mV]	J_{SC} [mA cm^{-2}]	FF	PCE [%]
60	779	3.35	0.68	1.78
80	905	16.89	0.70	10.64
100	938	18.37	0.68	11.66
150	807	17.96	0.64	9.66
175	755	15.66	0.70	8.52
200	589	1.38	0.67	0.56

As the annealing temperature is increased further above 100 °C, the V_{OC} is observed to decrease significantly, leading to a fall in PCE. The J_{SC} remains high up to an annealing temperature of 150 °C (17.96 mA cm^{-2}) before it too decreases. This trend can be explained by the formation of PbI_2 at these high temperatures instead of perovskite as seen in the UV-vis and the XRD measurements. As a consequence the light harvesting abilities of the material is reduced, resulting in the decrease in J_{SC} and V_{OC}. The trend in the J_{SC} is reflected in the UV-vis absorption and the incident-photon-to-current conversion efficiency (IPCE) (Supporting Information Figure S4) spectra measured for the samples. The IPCE spectral shape is similar for samples annealed at 60 to 100 °C, and in good agreement to that reported for the $CH_3NH_3PbI_3$ perovskite.[8] The intensity of the IPCE response reflects the amount of perovskite formed and hence is a measure of the extent of perovskite conversion, lowest for devices annealed at 60 °C and highest for 100 °C. Higher annealing temperatures not only lead to a decrease in the IPCE intensity but also to a change in the spectral shape, displaying a decrease in the region between 400 and 650 nm. This is attributed to the competitive light absorption from the additional formation of PbI_2.

2.5. Impedance Spectroscopy

In order to determine the origin for the decrease in the V_{OC} of the devices as the temperature for the perovskite annealing is increased from 100 °C, impedance spectroscopy (IS) measurements were conducted on the completed devices. This technique provides valuable insight into the internal electrical parameters of the solar cells under working conditions.

Using the model developed in our previous work,[33] the impedance data were fitted accordingly. The high frequency feature corresponding to the charge transfer resistance between the back contact and the HTM, as well as any charge transport

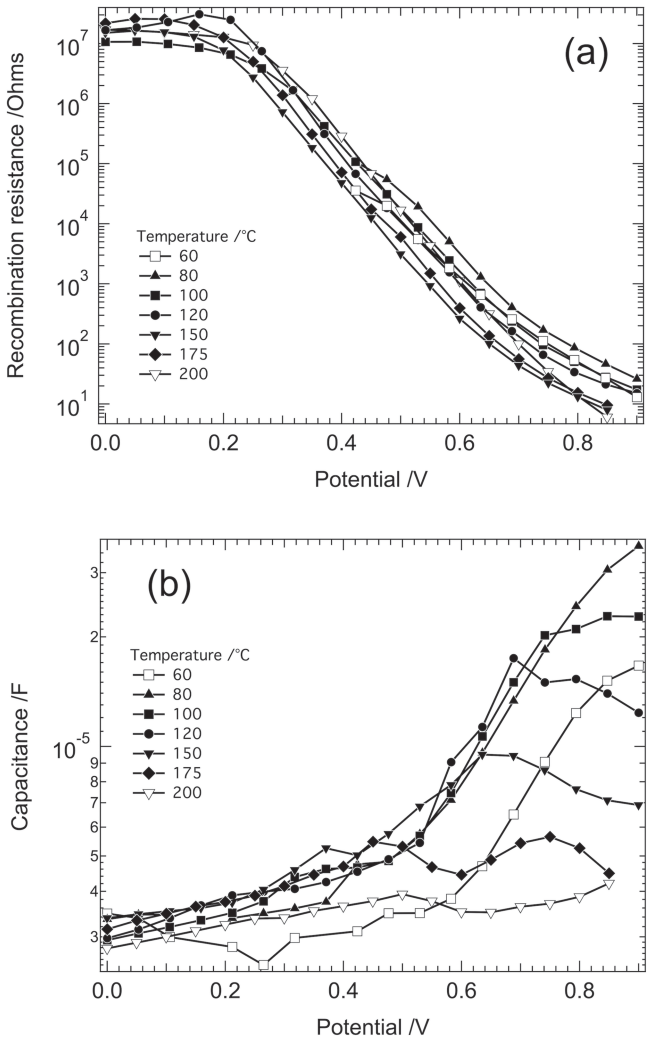

Figure 5. a) Recombination resistance and b) associated chemical capacitance determined from impedance spectroscopy measurements conducted on devices in the dark.

resistance within the HTM (if insufficiently doped) was found to remain more or less unchanged regardless of the annealing temperature used. This work focused on the intermediate to low frequency region in which the transport and recombination of charges manifests. **Figure 5** shows the recombination resistance, R_{ct} and associated chemical capacitance, C_{μ} determined from the impedance measurements conducted on devices in the dark. As can be seen the behavior of the recombination resistance remains relatively similar for all devices, no matter the annealing temperature used. This however is not the case for the chemical capacitance.

In the case where the perovskite was heated at 80 °C the chemical capacitance shows the typical behavior expected of such devices. At low forward bias, where the mesoporous TiO_2 is insulating and the charges flow through the compact TiO_2 underlayer, the associated capacitance of this interface is low. As the applied bias increases and the mesoporous TiO_2 becomes conductive (usually at an applied bias >400 mV), the chemical capacitance increases exponentially. This exponential behavior of the chemical capacitance is characteristic for such nanostructured materials and has been extensively reported.[34–37]

In the region of low forward bias, where the current flows over the blocking underlayer, the behavior of the chemical capacitance is similar for all devices, exhibiting a small increase in capacitance with increasing forward bias. As in the other measurements, the samples prepared at 100 °C and 80 °C behave relatively similar, with the exception that at very high forward bias, the chemical capacitance for the device annealed at 100 °C does not continue to increase, but instead shows a leveling off. Increasing the temperature further shows that the chemical capacitance deviates from its exponential increase at progressively lower forward bias. While for samples heated at 175 °C the chemical capacitance still shows some initial increase before remaining constant, annealing the perovskite at 200 °C resulted in the chemical capacitance displaying no considerable increase at all.

In the case of bulk heterojunctions devices, the capacitance has been observed to behave similarly, here the decrease of the capacitance at high forward applied bias was attributed to the formation of an injection limitation.[38,39] These types of devices show Schottky diode behavior at the metal-semiconductor contact. For Schottky diodes, the barrier height of this junction can limit the injection of the minority carrier under moderate to large forward bias thus determining the minority carrier concentration in the bulk semiconductor material.[40] Due to this injection limitation the charge collection is reduced and leads to the formation of a peak in the capacitance instead of increasing indefinitely with increasing forward bias. Furthermore this might evolve into a strong negative capacitive component.[40]

In the systems under consideration here injection of electrons from and to the $mTiO_2$ is dependent on the energy level alignment between the conduction bands of the $mTiO_2$ and the perovskite material. The conduction band (CB) energy for the perovskite material has been reported to be only very slightly higher than that of $mTiO_2$ (–3.93 eV and –4.00 eV below vacuum level for the perovskite and TiO_2 respectively).[2] Hence any upward shift of the CB of TiO_2 or downward shift of the CB of the perovskite would result in an injection barrier and thus prevent charge build up in the $mTiO_2$.

When high forward bias is applied in the dark, the CB in the $mTiO_2$ is unpinned. The upward shift of the CB of the $mTiO_2$ at high forward bias will lead to a misalignment of the energy levels. The behavior of the chemical capacitance was observed to be similar under illumination, while the recombination resistance showed the expected decrease in magnitude (see Supporting Information Figure S5).

A misalignment of the bands could possibly arise due to the increasing proportion of PbI_2 that forms with increasing annealing temperature. It is possible that the PbI_2 acts as a sink for charges injected from the perovskite, preventing the buildup within the $mTiO_2$ and accounting for the energy level misalignment. This is clearly shown in the case for samples annealed at 200 °C which contain a high proportion of PbI_2. The capacitance does not show any significant increase indicating that there is no injection from and into the $mTiO_2$ and thus no buildup of charges in the $mTiO_2$.

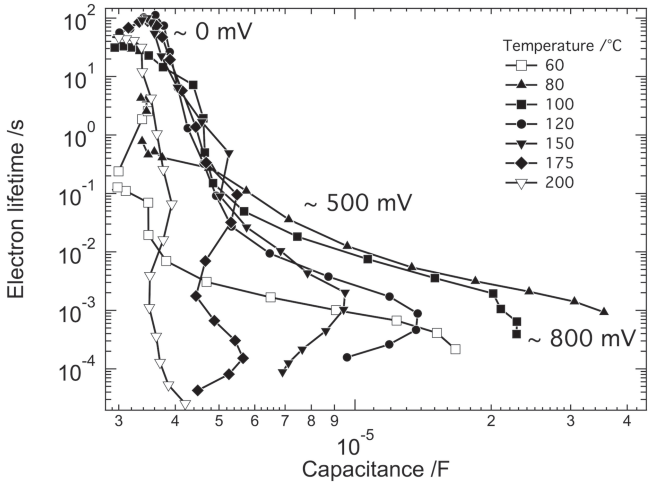

Figure 6. Electron lifetime calculated as described from the impedance spectroscopic measurements.

The peak in the chemical capacitance, before the observed decrease at high forward bias occurs at lower applied potential as the annealing temperature of the perovskite is increased. This indicates that the misalignment of the energy levels and the formation of a barrier at the $mTiO_2$ occur at lower applied forward bias.

The chemical capacitance is directly proportional to the density of trap states (DOS) within the $mTiO_2$. **Figure 6** shows the electron lifetime plotted against the chemical capacitance, thus allowing for direct comparison of the lifetimes at similar DOS. The electron lifetime, τ_n can be determined from the chemical capacitance and the recombination, $\tau_n = C_\mu \times R_{ct}$.

As can be seen from Figure 6 the electron lifetime decreases as the annealing temperature is increased from 80 to 200 °C. This clearly reflects the evolution of the open-circuit potential extracted from the *J-V* characteristics for devices made using increasing annealing temperatures. These displayed an initial increase in V_{OC} as the annealing temperature increased up to 100 °C corresponding to incomplete conversion to the perovskite material at low temperatures. This was subsequently followed by a decrease in V_{OC} as the annealing temperature is further increased. The electron lifetime of the devices was observed to be longest for devices annealed at 80 and 100 °C, steadily decreasing as temperatures increase to 200 °C. Similarly devices treated at 60 °C also showed a lower electron lifetime, arising from the incomplete conversion of the precursors to the perovskite material.

From the observations made from the IS measurements it is possible to deduce that the heat treatment of the perovskite precursors at too high temperatures changes the energy levels within the formed perovskite material in such a way as to hinder the electron injection from and into the $mTiO_2$ at high forward bias. It remains unclear whether this is due to the change in morphology of the formed perovskite film or due to the increasing proportion of PbI_2 formed. Finally the perovskite material itself may influence the conduction band position of the mesoporous TiO_2.

3. Conclusions

In this work, we investigated the role of the annealing temperature used in the conversion process to form the perovskite material from the deposited precursor solution. This parameter was found to have critical impact on the formed perovskite film morphology and thus the power conversion efficiency of the solar cells fabricated. The film morphology was examined by UV-vis spectroscopy, SEM imaging and XRD, which all indicate that a minimum temperature of 80 °C is required to sufficiently form the $CH_3NH_3PbI_3$ perovskite. Using lower temperatures or simply drying the $mTiO_2$ film after the perovskite precursor solution is deposited leads to incomplete conversion. These low temperatures remove the solvent from the solution, leaving the dried precursors on the film, but are insufficient to lead to the perovskite formation, thus indicating that there is an energy requirement (endothermic reaction) to the formation of the perovskite. On the other hand as the perovskite annealing temperature is increased, the film morphology undergoes clear changes forming distinct islands of materials on the surface of the film that display internal structuring as the temperature is increased further. This is accompanied by an increased amount of PbI_2 content in the film, as seen in the XRD measurements and in the UV-vis spectra.

These changes in film morphology are correlated with the photovoltaic performance of solid-state solar cells. The highest performance was achieved for devices fabricated using an annealing temperature between 80 and 100 °C, which corresponds to samples that showed complete conversion of the precursors to the perovskite, with no additional PbI_2 formation, as well as a film morphology consisting of a type of interconnected network of perovskite crystallites. Furthermore these conditions showed the highest absorbance (a direct result of the extent of perovskite conversion) leading to the highest short-current density.

IS spectroscopy was used to further examine the internal electrical processes within these devices and gain a better understanding of the role of the film morphology and perovskite conversion mechanism on the device performance. A clear trend in the chemical capacitance was observed. Increasing the annealing temperature of the perovskite led to deviation from the typical exponential behavior of the chemical capacitance at high forward bias. This is believed to be due to a misalignment of the energy levels and the formation of a barrier at the $mTiO_2$ at high forward bias. This effect becomes more dominant and occurs at lower forward applied bias as the annealing temperature is increased, until the capacitance is observed to not increase at all for the devices with the perovskite annealed at 200 °C. This can be correlated with the increasing PbI_2 content within the perovskite material and the increasing size of the perovskite crystallite islands formed on the $mTiO_2$ film. The formation of PbI_2 at higher annealing temperatures may moreover act as a sink for the charges, thus limiting the injection of charges to and from the $mTiO_2$.

Hence, in this investigation, we have highlighted the importance of the perovskite formation mechanism on the perovskite film morphology and consequently on the solar cell device performance, through intensive characterization of the perovskite film formed and of the solar cells fabricated. We

have investigated only the influence of one parameter, the annealing temperature used in the conversion process in the one-step method from a perovskite precursor solution of $PbCl_2$ and CH_3NH_3I (1:3 molar ratio) in DMF. While the film morphology of the perovskite is highly dependent on the deposition techniques and the precursor solutions used as previously stated, the additional formation of the PbI_2 at higher annealing temperatures and the associated trends observed in the device photovoltaic performance and working mechanisms is believed to be general for the $CH_3NH_3PbI_3$ perovskite, regardless of the deposition process. In order to achieve high power conversion efficiencies, it is necessary to not only consider the choice of deposition technique, but also the conditions the perovskite film is treated and/or exposed to. In this study the annealing process was found to be critical in the perovskite film formation and consequently on the power conversion efficiency of the ensuing devices assembled.

4. Experimental Section

Materials: All chemicals purchased from Sigma-Aldrich were used as received. The hole transport material, Spiro-MeOTAD (2,2′,7,7′-tetrakis(*N*,*N*-di-*p*-methoxy-phenylamine)-9,9′-spirobifluorene) was purchased from Merck and used as received. CH_3NH_3I was synthesized in our laboratory.

Device Fabrication: The desired electrode configuration was laser etched onto fluorine-doped tin-oxide (FTO) coated glass substrates (TEC 15, Pilkington), which were then cleaned by mechanical scrubbing with Hellmanex, ultrasonification and ozone cleaning. The TiO_2 blocking underlayer was deposited by spray pyrolysis at 450 °C of the precursor solution, diisopropoxide bis(acetylacetonate) diluted in ethanol (1:20 volume ratio), using oxygen as a carrier gas. The films were exposed to a $TiCl_4$ treatment using an aqueous solution of $TiCl_4$ (20 mM) for 30 min at 70 °C before sintering at 500 °C for 20 min. TiO_2 paste (Dyesol 18NR-T) was diluted by ethanol at 1:3.5 by weight and deposited on the substrates by spin-coating at 5000 rpm for 30 s prior to stepwise heating to 500 °C at which they were sintered for 15 min. Immediately afterwards the mesoporous TiO_2 ($mTiO_2$) films were transferred into a dry box and all following deposition processes were conducted under dry atmosphere (less than 5% humidity). The perovskite precursor solution was prepared as reported by Lee et al.[4] $PbCl_2$ and CH_3NH_3I were dissolved in dimethylformamide in a 1:3 molar ratio. This solution was deposited on the $mTiO_2$ by spin-coating at 2000 rpm for 30 s and then heat treated at different temperatures as described in the manuscript, Table 1. The hole transport material (HTM) solution consisted of spiro-MeOTAD (0.05 M) dissolved in chlorobenzene, oxidized by the addition of 5% molar ratio of cobalt(III) dopant, tris(2-(1*H*-pyrazol-1-yl)-4-tert-butylpyridine)cobalt(III)-tris(bis(trifluoro-methyl-sulfonyl)-imide)), coded FK209. Finally *tert*-butylpyridine (TBP) (0.2 M) and $Li[(CF_3SO_2)_2N]$ (LiTFSI) (0.03 M) were added. The HTM solution was deposited on the perovskite sensitized films by spin-coating at 2000 rpm for 30 s. Thermal evaporation was used to deposit Au (60 nm) for the back contact. The complete device fabrication was conducted under controlled dry conditions with humidity levels of less than 5%. The devices were not sealed but stored in dry, dark conditions and measured in normal ambient atmosphere.

Ultraviolet-Visible Absorption Spectroscopy: The UV-vis absorption spectra were recorded with a Varian Cary 5 spectrophotometer in transmission mode. The samples consisted of microscopic glass slides onto which the $mTiO_2$ followed by the perovskite was deposited as described above.

X-Ray Diffraction: The perovskite samples were deposited onto films of $mTiO_2$ on FTO coated glass substrates following the procedure above. The X-ray powder diagrams were recorded on a X'Pert MPD PRO (Panalytical) operated in BRAGG-BRENTANO geometry, using a RTMS X'Celerator detector, a ceramic tube (Cu anode, λ = 1.54060 Å) and a secondary graphite (002) monochromator. No further modification was made to mount to the samples and adjustments were made to the automatic divergence slit and the beam mask to account for the dimensions of the sample films. An acquisition time of 7.5 min deg^{-1} was employed with a step size of 0.008°.

Photovoltaic Characterization: The current-voltage characteristics were determined using a digital source meter (Keithley Model 2400) to apply an external potential bias to the solar cells and measuring the generated photocurrent. The emission spectrum from a 450 W xenon lamp (Oriel) was matched to the standard AM1.5G using a Schott K113 Tempax sunlight filter (Praezisions Glas & Optik GmbH). The exact light intensities of the measurements were determined using a calibrated Si diode as reference. The IPCE spectra were recorded as a function of the wavelength using a Model SR830 DSP Lock-In Amplifier (Stanford Research Systems). The excitation beam was provided by a 300 W Xenon lamp (ILC technology), focused through a Gemini-180 double monochromator (Jobin Yvon Ltd.) and chopped at approximately 2 Hz.

Impedance Spectroscopy: A Bio-Logic SP300 potentiostat was used to conduct the impedance measurements. A sinusoidal AC potential perturbation of 15 mV was overlaid on an applied DC potential bias over a frequency range of 7 MHz to 0.1 Hz. The applied DC potential bias was step wise changed by approximately 50 mV from 850 to 0 mV. Measurements were conducted in the dark and under illumination using an LED light source. The ZView software (Scribner Associates Inc.) was used to fit the impedance spectra.

Supporting Information

Supporting Information is available from the Wiley Online Library or from the author.

Acknowledgements

The authors would like to thank K. Schenk and N. Pellet for the XRD measurements. The authors acknowledge financial support from Aisin Cosmos R&D Co., Ltd, Japan, from the European Community's Seventh Framework Programme (FP7/2007–2013) under the "ORION" grant agreement no. NMP-229036 and from the European Research Council Advanced Research Grant (ARG 247404) under the "Mesolight" project.

Received: November 29, 2013
Revised: December 19, 2013
Published online: February 13, 2014

[1] J.-H. Im, C.-R. Lee, J.-W. Lee, S.-W. Park, N.-G. Park, *Nanoscale* **2011**, *3*, 4088.
[2] H.-S. Kim, C.-R. Lee, J.-H. Im, K.-B. Lee, T. Moehl, A. Marchioro, S.-J. Moon, R. Humphry-Baker, J.-H. Yum, J.-E. Moser, M. Grätzel, N.-G. Park, *Nature* **2012**, *2*.
[3] I. Chung, B. Lee, J. He, R. P. H. Chang, M. G. Kanatzidis, *Nature* **2012**, *485*, 486.
[4] M. M. Lee, J. Teuscher, T. Miyasaka, T. N. Murakami, H. Snaith, *Science* **2012**, *338*, 643.
[5] J. M. Ball, M. M. Lee, A. Hey, H. Snaith, *Energy Environ. Sci.* **2013**, *6*, 1739.
[6] B. M. Kim, S. G. Rho, C. H. Kang, *J. Nanosci. Nanotechnol.* **2011**, *11*, 1515.
[7] L. Etgar, P. Gao, Z. Xue, Q. Peng, A. K. Chandiran, B. Liu, M. K. Nazeeruddin, M. Grätzel, *J. Am. Chem. Soc.* **2013**, *134*, 17396.

[8] J. Burschka, N. Pellet, S.-J. Moon, R. Humphry-Baker, P. Gao, M. K. Nazeeruddin, M. Grätzel, *Nature* **2013**.
[9] D. Bi, L. Häggman, G. Boschloo, L. Yang, E. M. J. Johansson, A. Hagfeldt, *RSC Adv.* **2013**.
[10] H.-S. Kim, I. Mora-Sero, V. Gonzalez-Pedro, F. Fabregat-Santiago, E. J. Juarez-Perez, N.-G. Park, J. Bisquert, *Nat. Commun.* **2013**, *4*.
[11] Y. Zhao, K. Zhu, *J. Phys. Chem. Lett.* **2013**, *4*, 2880.
[12] E. Edri, S. Kirmayer, D. Cahen, G. Hodes, *J. Phys. Chem. Lett.* **2013**, *4*, 897.
[13] D. Bi, L. Yang, G. Boschloo, A. Hagfeldt, E. M. J. Johansson, *J. Phys. Chem. Lett.* **2013**, *4*, 1532.
[14] J. H. Heo, S. H. Im, J. H. Noh, T. N. Mandal, C.-S. Lim, J. A. Chang, Y. H. Lee, H.-J. Kim, A. Sarkar, M. K. Nazeeruddin, M. Grätzel, S. I. Seok, *Nat. Photonics* **2013**, *7*, 486.
[15] Z. Cheng, J. Lin, *Cryst. Eng. Commun.* **2010**, *12*, 2646.
[16] D. B. Mitzi, C. A. Feild, W. T. A. Harrison, A. M. Guloy, *Nature* **1994**, *369*, 467.
[17] D. B. Mitzi, K. Chondroudis, C. R. Kagan, *Inorg. Chem* **1999**, *38*, 6246.
[18] K. Chondroudis, D. B. Mitzi, *Chem. Mater.* **1999**, *11*, 3028.
[19] C. Kagan, D. Mitzi, C. Dimitrakopoulos, *Science* **1999**, *286*, 945.
[20] J. Flocken, R. Guenther, J. Hardy, L. Boyer, *Phys. Rev. B* **1985**, *31*, 7252.
[21] M. Liu, M. B. Johnston, H. Snaith, *Nature* **2013**.
[22] T. Supasai, N. Rujisamphan, K. Ullrich, A. Chemseddine, T. Dittrich, *Appl. Phys. Lett.* **2013**, *103*, 183906.
[23] A. M. Pollard, *Mineralog. Mag.* **1992**, *56*, 53.
[24] A. Kojima, K. Teshima, Y. Shirai, T. Miyasaka, *J. Am. Chem. Soc.* **2009**, *131*, 6050.
[25] T. Baikie, Y. Fang, J. M. Kadro, M. Schreyer, F. Wei, S. G. Mhaisalkar, M. Grätzel, T. J. White, *J. Mater. Chem. A* **2013**, *1*, 5628.
[26] A. Poglitsch, D. Weber, *J. Chem. Phys.* **1987**, *87*, 6373.
[27] S. Colella, E. Mosconi, P. Fedeli, A. Listorti, F. Gazza, F. Orlandi, P. Ferro, T. Besagni, A. Rizzo, G. Calestani, G. Gigli, F. De Angelis, R. Mosca, *Chem. Mater.* **2013**, *25*, 4613.
[28] M. Ishihara, S. J. Li, H. Yumoto, K. Akashi, Y. Ide, *Thin Solid Films* **1998**, *316*, 152.
[29] M. Ohyama, H. Kouzuka, T. Yoko, *Thin Solid Films* **1997**, *306*, 78.
[30] Y. Xu, J. S. Chen, J. P. Wang, *Appl. Phys. Lett.* **2002**, *80*, 3325.
[31] P. A. Beckmann, *Cryst. Res. Technol.* **2010**, *45*, 455.
[32] C. C. Stoumpos, C. D. Malliakas, M. G. Kanatzidis, *Inorg. Chem* **2013**, *52*, 9019.
[33] A. Dualeh, T. Moehl, N. Tétreault, J. Teuscher, P. Gao, M. K. Nazeeruddin, M. Grätzel, *ACS Nano* **2013**, *8*, 362.
[34] J. Bisquert, *Phys. Chem. Chem. Phys.* **2003**, *5*, 5360.
[35] Q. Wang, S. Ito, M. Grätzel, F. Fabregat-Santiago, I. Mora-Sero, J. Bisquert, T. Bessho, H. Imai, *J. Phys. Chem. B* **2006**, *110*, 25210.
[36] J. Bisquert, D. Cahen, G. Hodes, S. Rühle, A. Zaban, *J. Phys. Chem. B* **2004**, *108*, 8106.
[37] J. Bisquert, F. Fabregat-Santiago, I. Mora-Sero, G. Garcia-Belmonte, S. Gimenez, *J. Phys. Chem. C* **2009**, *113*, 17278.
[38] J. Bisquert, G. Garcia-Belmonte, A. Munar, M. Sessolo, A. Soriano, H. J. Bolink, *Chem. Phys. Lett.* **2008**, *465*, 57.
[39] G. Garcia-Belmonte, A. Munar, E. M. Barea, J. Bisquert, I. Ugarte, R. Pacios, *Org. Electron.* **2008**, *9*, 847.
[40] M. A. Green, J. Shewchun, *Solid-State Electron.* **1973**, *16*, 1141.